Energetics and dynamics of a light-driven sodium-pumping rhodopsin

Suomivuori, Carl-Mikael

2017-07-03

Suomivuori , C-M , Gamiz-Hernandez , A P , Sundholm , D & Kaila , V R I 2017 , ' Energetics and dynamics of a light-driven sodium-pumping rhodopsin ' , Proceedings of the National Academy of Sciences of the United States of America , vol. 114 , no. 27 , pp. 7043-7048 . https://doi.org/10.1073/pnas.1703625114

http://hdl.handle.net/10138/305655
https://doi.org/10.1073/pnas.1703625114

other
publishedVersion

Energetics and dynamics of a light-driven sodium-pumping rhodopsin

Carl-Mikael Suomivuori[a,b], Ana P. Gamiz-Hernandez[b], Dage Sundholm[a], and Ville R. I. Kaila[b,1]

[a]Department of Chemistry, University of Helsinki, FIN-00014 Helsinki, Finland; and [b]Department Chemie, Technische Universität München, D-85747 Garching, Germany

Edited by Arieh Warshel, University of Southern California, Los Angeles, CA, and approved May 19, 2017 (received for review March 3, 2017)

The conversion of light energy into ion gradients across biological membranes is one of the most fundamental reactions in primary biological energy transduction. Recently, the structure of the first light-activated Na^+ pump, *Krokinobacter eikastus* rhodopsin 2 (KR2), was resolved at atomic resolution [Kato HE, et al. (2015) *Nature* 521:48–53]. To elucidate its molecular mechanism for Na^+ pumping, we perform here extensive classical and quantum molecular dynamics (MD) simulations of transient photocycle states. Our simulations show how the dynamics of key residues regulate water and ion access between the bulk and the buried light-triggered retinal site. We identify putative Na^+ binding sites and show how protonation and conformational changes gate the ion through these sites toward the extracellular side. We further show by correlated ab initio quantum chemical calculations that the obtained putative photocycle intermediates are in close agreement with experimental transient optical spectroscopic data. The combined results of the ion translocation and gating mechanisms in KR2 may provide a basis for the rational design of novel light-driven ion pumps with optogenetic applications.

bacterial ion pumps | bioenergetics | QM/MM | optogenetics | retinal

Primary biological energy conversion is based on the efficient capture and conversion of light and chemical energy into ion gradients across biological membranes (1, 2). The established gradients are used to thermodynamically drive energy-requiring processes, such as active transport and synthesis of adenosine triphosphate (ATP) (3, 4). The rhodopsin family of proteins catalyzes such reactions by harnessing the energy from retinal photoisomerization and deprotonation reactions, followed by conformational changes that further trigger the pumping of ions across the membrane (5). All previously known ion-pumping rhodopsins function either as inward chloride or outward proton pumps, but the structure of the first Na^+ pumping rhodopsin, *Krokinobacter eikastus* rhodopsin 2 (KR2) (6), was recently resolved (7, 8). In the absence of Na^+ ions, KR2 functions as an outward proton pump, similarly to bacteriorhodopsin (bR), but under physiological conditions, KR2 pumps Na^+ out of the cell (6, 9).

KR2 shares the heptahelical transmembrane (7TM) structure common to all microbial rhodopsins (Fig. 1*A*) (5, 7, 8). In contrast to bR, however, where a highly conserved Asp–Thr–Asp (DTD) motif is used to pump protons, KR2 employs a unique NDQ motif comprising residues Asn112, Asp116, and Gln123 (6). In bR, Asp85 and Asp96 function as proton acceptors and donors for the protonated Schiff base (PSB), respectively, whereas in KR2, Asn112 and Gln123 occupy these positions, and Asp116 replaces Thr89. In analogy to bR, it has been suggested that Gln123 aids in capturing ions from the solvent and that Asn112 might be part of a Na^+ binding site (6, 10).

Similarly to other microbial rhodopsins, four photocycle intermediates have been spectroscopically identified in KR2 (Fig. 1*B*) (6), although their structure remains unclear. The X-ray structure of the resting state of KR2 (7, 8) suggests that the all-*trans* retinal Schiff base is protonated and its counterion, Asp116, is deprotonated (Fig. 1*A*). Upon photoexcitation, the retinal isomerizes to the 13-*cis* form, leading to the redshifted K intermediate, followed by a preequilibrium between the subsequent L and M states (Fig. 1*B*) (6). The blueshifted absorption of the M intermediate indicates that the Schiff base proton is transferred to Asp116, whereas reprotonation of the retinal results in the redshifted O intermediate, which finally relaxes back to the resting KR2 state. Experimental studies (6, 11, 12) indicate that the Na^+ uptake and release likely occurs upon the decay of the L/M and O intermediates, respectively (Fig. 1*B*).

The mechanism of Na^+ pumping in KR2 presents a unique challenge, as the positively charged retinal in the middle of the channel is expected to impede the transport of cations other than protons (7). Furthermore, mechanistic studies of the Na^+ pumping in KR2 have important neurophysiological applications, as the protein can be used as an inhibitory optogenetic tool, which does not affect the pH balance of the organism (6, 7, 13, 14). Despite several experimental studies (11, 15–18), as well as the recently resolved X-ray structure (7, 8), the exact molecular mechanism by which KR2 pumps Na^+ remains elusive.

In this work, we show by classical atomistic molecular dynamics (MD) simulations and hybrid quantum mechanics/molecular mechanics (QM/MM) calculations how conformational, electrostatic, and hydration changes lead to transfer of the Na^+ ion across the membrane. Our calculations identify putative ion-binding sites that can stimulate site-directed mutagenesis experiments. We also suggest putative structures for the transient photocycle intermediates, which we verify based on calculations of absorption spectra. Understanding the molecular mechanism of light-driven Na^+ transport by KR2 is essential for the rational design of novel light-driven ion pumps that hyperpolarize the membrane potential and could be used as inhibitory optogenetic tools (6, 7, 13, 14).

Results and Discussion

Structure and Dynamics of Photocycle Intermediates in KR2. To probe the dynamics of KR2 during the photocycle, we performed in total ∼32 μs of atomistic MD simulations (*SI Appendix*, Table S1)

Significance

***Krokinobacter eikastus* rhodopsin 2 (KR2) is the first identified light-driven Na^+ pump. Despite its recently resolved X-ray structure, the molecular mechanism of the translocation and gating of Na^+ ions during its photocycle has remained elusive. Here we use large-scale quantum and classical simulations to prepare KR2 in transient photocycle states and show how combined electrostatic, conformational, and hydration changes drive the Na^+ ions across the membrane. Our calculations identify putative ion-binding sites that can be further probed by site-directed mutagenesis experiments. The obtained results provide rational design principles to develop KR2 toward next generation optogenetic tools.**

Author contributions: C.-M.S. and V.R.I.K. designed research; C.-M.S., A.P.G.-H., and V.R.I.K. performed research; C.-M.S. and A.P.G.-H. contributed new reagents/analytic tools; C.-M.S., A.P.G.-H., D.S., and V.R.I.K. analyzed data; and C.-M.S. and V.R.I.K. wrote the paper.

The authors declare no conflict of interest.

This article is a PNAS Direct Submission.

Freely available online through the PNAS open access option.

[1]To whom correspondence should be addressed. Email: ville.kaila@ch.tum.de.

This article contains supporting information online at www.pnas.org/lookup/suppl/doi:10.1073/pnas.1703625114/-/DCSupplemental.

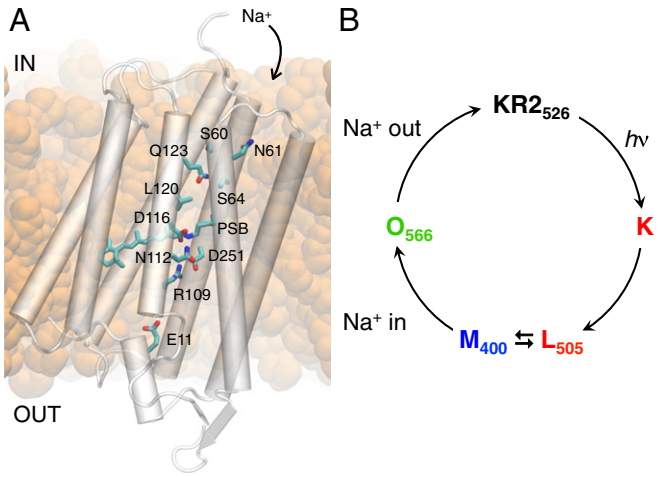

Fig. 1. (*A*) The overall structure, key residues, and the protonated Schiff base (PSB) retinal of KR2 in the resting state. KR2 pumps Na^+ from the intracellular cytoplasm (IN) to the extracellular side of the membrane (OUT). (*B*) The photocycle of KR2 consists of the sequentially forming K, L/M, and O intermediates, with the subscripts denoting observed absorption maxima in nanometers.

of the X-ray structure (7) embedded in a water–membrane–ion environment. Our 1.5-μs MD simulation of the resting KR2 state shows hydration of internal cavities on the intra- and extracellular sides, but the connectivity between the retinal and the cytoplasm is broken by Leu120 (Fig. 2*A* and *SI Appendix*, Fig. S1), which is conserved among H^+-pumping microbial rhodopsins (7, 19, 20) and is also found in the Cl^- pump *Nonlabens marinus* rhodopsin 3 (NM-R3) (21, 22). The hydrated cavity on the intracellular side contains Gln123 of the NDQ motif, as well as Asn61, which plays a role in the ion selectivity (7, 23). The hydrophilic residues Ser60 and Ser64 also reside in this cavity (Fig. 2*A*). A hydrated cavity also forms on the extracellular side, ∼5 Å from the retinal, and it contains Asn112, of the NDQ motif, as well as the conserved residues Asp251 and Arg109 (Fig. 2*A*), both of which have been found to be essential for Na^+ pumping (6, 7). Moreover, Glu11, located near the extracellular bulk, becomes extensively hydrated and could thus form a part of the Na^+ translocation pathway (Fig. 2*A*).

To derive a structural model for the K/L state, we isomerized the retinal to the 13-*cis* form and reinitiated the MD simulations. During the MD trajectories of this state, the Schiff base proton initially points away from Asp116, but the contact between the PSB and the latter reforms within 10–50 ns, due to the conformational flexibility of the two side chains (*SI Appendix*, Fig. S2). However, in stark contrast to the resting state, where the side chain of Asp116 remains parallel to the N-H Schiff base bond vector, Asp116 flips in the K/L state toward the intracellular side of the retinal, while still remaining hydrogen bonded to the PSB (Fig. 2*A*). This flipping induces an electrostatic potential energy change of ∼50 meV at the opening of the intracellular cavity (Fig. 2*B*), which could attract Na^+ from the cytosol toward the center of the channel (see also below *Energetics of Na^+ Translocation*). Moreover, in contrast to the resting state, a water cluster forms in the K/L state between the PSB and the intracellular water cavity (Fig. 2*A*). The formation of hydrogen-bonded water chains is known to be essential for the function of bR (24, 25), and the observed hydrated structures are therefore most likely of functional relevance in KR2. This hydration event correlates with the motion of Leu120, which flips away from the retinal (Fig. 2*C*), allowing water access to the PSB. These findings strongly suggest that Leu120 may act as a hydrophobic gate in KR2, consistent with suggestions made by Guschin et al. (8). The gating function of Leu120 is further supported by the dynamics of the homologous Leu93 in bR, which also shows a flipping behavior (26). Although mutations at Leu120 have not been experimentally studied in KR2 (*SI Appendix*, Table S2), the photocycle is slowed down by a factor of 100 in the L93A and L93T mutants of bR (27).

To probe the dynamics of the M state, we transferred the proton from the PSB to Asp116 in the K/L state and initiated new MD simulations. In this state, the protonated Asp116 flips within 30–300 ns away from the neutral retinal [Schiff base (SB)], forming a hydrogen bond with Asn112 and Ser70 (Fig. 2*A* and *SI Appendix*, Fig. S2). Interestingly, Kato et al. (7) also found that these residues form contacts with Asp116 in crystal structures obtained under acidic conditions. The flipping of Asp116 occurs concertedly with the closing motion of Leu120, which reforms its resting state

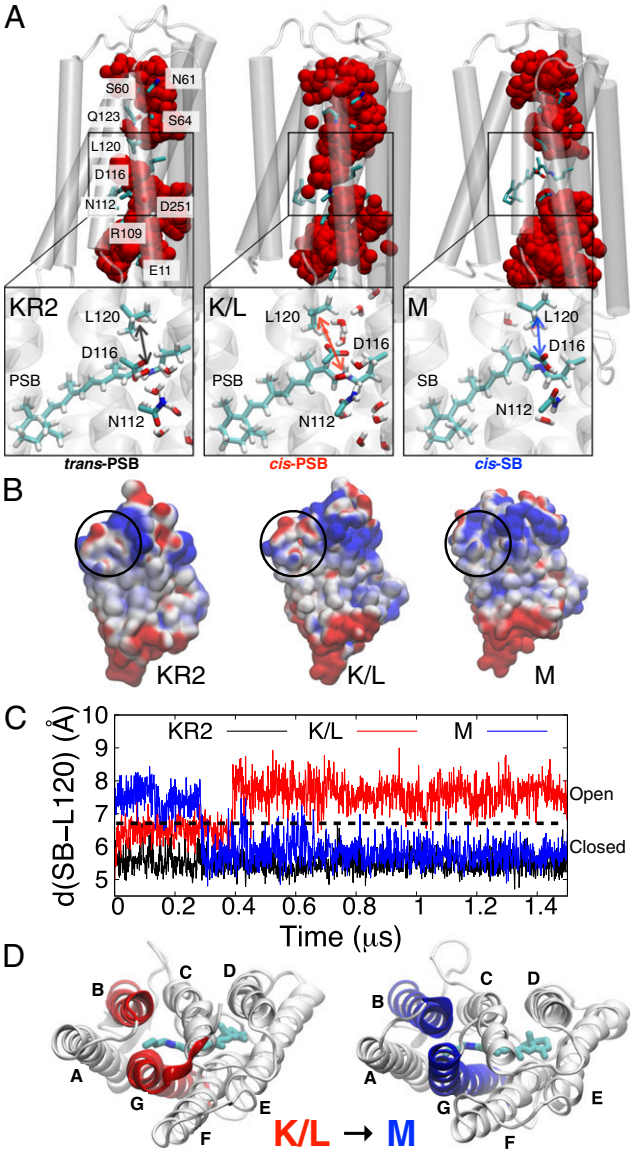

Fig. 2. (*A*) Hydration of internal protein cavities of the photocycle intermediates KR2, K/L, and M. Water molecule positions from every 10 ns during the final 1.0 μs of the MD simulations are shown as red van der Waals spheres. In the resting KR2 and M states, the water connectivity is broken between the cytoplasm and the extracellular side by Leu120. *Insets* show snapshots of the retinal region. (*B*) Electrostatic potential surface for the different intermediates, with circles marking the entrance of the intracellular cavity. Color scale is as follows: +1 *kT/e* in blue; −1 *kT/e* in red. (*C*) Distance between Leu120 (atom CG) and the Schiff base nitrogen (SB) in the photocycle states. (*D*) Helix movement in the K/L → M transition as seen from the intracellular side.

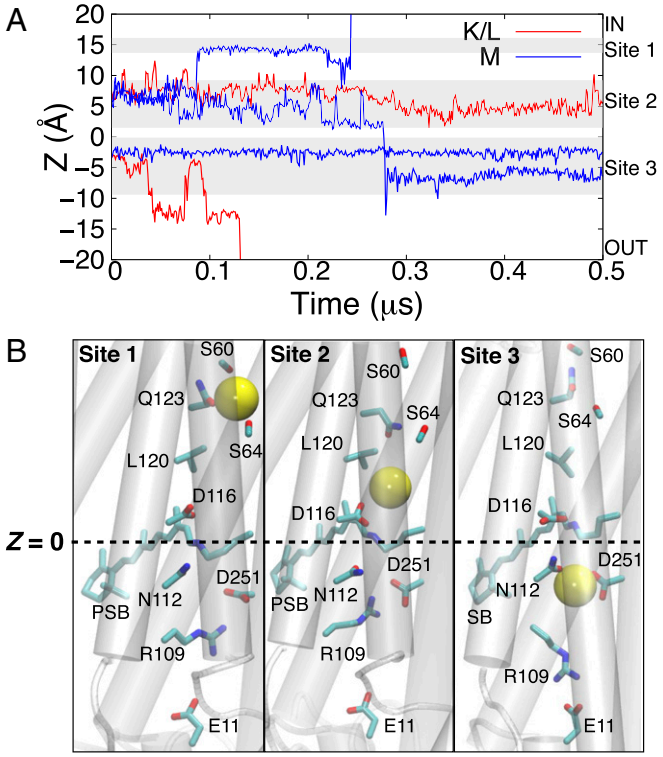

Fig. 3. (*A*) Dynamics of Na^+ in different photocycle states. The *Z* coordinate is the distance of the Na^+ ion perpendicular to the membrane plane, with the center of the membrane located at $Z = 0$. Statistics of all simulations are shown in *SI Appendix*, Fig. S4. (*B*) Putative Na^+ binding sites. (*Left*) Site 1, comprising residues Ser60, Ser64, and Gln123 in the K/L state. (*Center*) Site 2, comprising the counterion, Asp116, in the K/L state. (*Right*) Site 3, comprising Asn112/Asp251 in the M intermediate. All binding sites are partially hydrated, whereas site 2 becomes extensively hydrated in the K/L state. Coordination numbers in the different binding sites are shown in *SI Appendix*, Fig. S6.

conformation (Fig. 2*C*), breaking the water connectivity between the retinal and the cytoplasm. Furthermore, the intracellular cavity dries up as helices B and G move closer together, inducing channel closure (Fig. 2*D* and *SI Appendix*, Fig. S3). Interestingly, light-induced movement of helices B and G has also been found to play an important role in the pore formation of channelrhodopsin (ChR) (28, 29). This helix movement correlates with a shift in the electrostatic potential at the opening of the intracellular cavity toward more positive values relative to the K/L state (Fig. 2*B*). These results suggest that Na^+ uptake should occur before the channel closing, i.e., in the K/L intermediate, or alternatively, in M before Leu120 has flipped. Experimental studies indeed indicate that Na^+ entry takes place in the L/M → O transition, because the rate of O formation is accelerated under higher NaCl concentrations (6).

Identification of Na^+ Translocation Pathways. To further probe the ion transport mechanism, we relaxed Na^+ ions at multiple internal sites that are hydrated during the MD simulations and reinitiated the simulations. We first probed whether the Na^+ ions spontaneously pass the retinal by placing Na^+ near Asp116 in the intracellular water cavity of the equilibrated K/L state. In five independent 0.5-μs simulations, the Na^+ ion remains trapped between Asp116 and Gln123 in the intracellular water cavity (site 2, Fig. 3 *A* and *B* and *SI Appendix*, Fig. S4*A*), suggesting that the electrostatic interaction between the PSB and Asp116 may act as a permeation barrier for the Na^+ translocation in the K/L state. Interestingly, the ion is not released back to the intracellular side in any of the five 0.5-μs simulations of the K/L state (*SI Appendix*, Fig. S4*A*). Solvation free-energy profiles (Fig. 4) suggest that the transfer of Na^+ from the bulk to Asp116 is exergonic by ∼5 kcal·mol^{-1}.

Starting with Na^+ in the intracellular water cavity near Asp116 in the K/L state, we then transferred the Schiff base proton to Asp116, forming the M state, and reinitiated the simulations. In stark contrast to the K/L state, we find that in one out of the five independent simulations, the ion passes the deprotonated retinal within 0.3 μs (Fig. 3 *A* and *B*, *SI Appendix*, Fig. S4*B*, and Movie S1). As the ion approaches Asp251, Arg109 flips toward Glu11 (Fig. 3*B* and *SI Appendix*, Fig. S5), located at the extracellular opening, after which the ion remains bound to Asp251 and Asn112 for the remaining 0.2 μs (site 3, Fig. 3*B*). Consistent with these results, it was observed in site-directed mutagenesis experiments that the N112A mutant is able to pump H^+, but has no Na^+ translocation activity (10). A recent study also found that out of 19 mutations at Asn112, only 4 retain Na^+ pumping activity (30), suggesting that Asn112 may contribute to the Na^+ binding. Interestingly, the Na^+ pumping activity is completely lost for the D251N mutant (6), supporting the role of this conserved residue in proton-pumping rhodopsins (5). In three other M state trajectories, the Na^+ ion does not pass the retinal, but binds instead to Ser60, Ser64, and Gln123, near the opening of the intracellular water cavity, before ultimately exiting to the cytoplasmic side of the membrane (site 1, Fig. 3 *A* and *B* and *SI Appendix*, Fig. S4*B*). These residues could thus serve as a transient Na^+ loading site, which is consistent with a decreased Na^+ pumping activity in the Q123V/A mutants (6, 7). Recently, it was also found that the Q123D/E mutations transform KR2 into an H^+ transporter (31), suggesting that Gln123 plays a central role in the Na^+ translocation. Moreover, Asn61, located next to this putative binding site, has been shown to be important for the ion selectivity (*SI Appendix*, Table S2) (7, 23). This transient binding site might not be accessible in the fully relaxed M intermediate, as Ser60 and Ser64 are part of helix B, which forms contacts with helix G in the relaxed M state (Fig. 2*D*). To our knowledge, the effects of mutations at the Ser60/Ser64 sites for Na^+ pumping have not been experimentally investigated (*SI Appendix*, Table S2).

Starting from the M state with a stable Na^+ ion at the Asn112/Asp251 site (site 3, Fig. 3*B* and *SI Appendix*, Fig. S4*D*), we reprotonated the retinal to probe the dynamics of the ions in the M → O transition. Remarkably, the Na^+ ion rapidly leaves the binding site within ∼0.1–0.3 μs in two out of five independent 0.5-μs simulations and exits to the extracellular side via Glu11 (Fig. 3*A*, *SI Appendix*, Fig. S4*C*, and Movie S2). After the Na^+ ion enters the

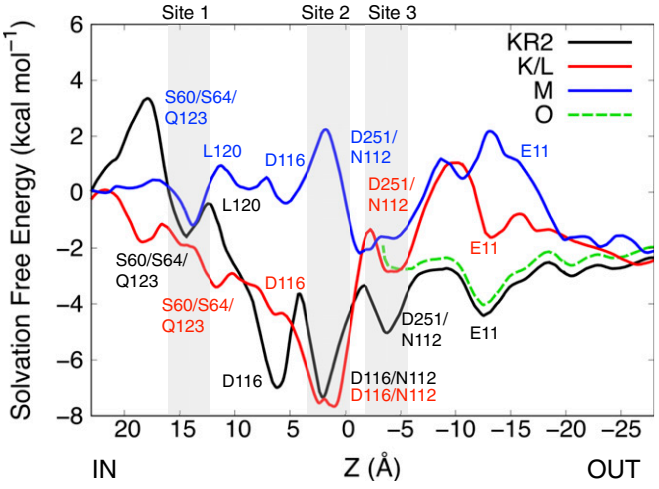

Fig. 4. Electrostatic solvation free-energy profiles for the Na^+ translocation through different photocycle states. Positive and negative *Z* coordinates refer to the intra- (IN) and extracellular (OUT) sides of the membrane.

bulk, Arg109 flips back toward Asp251, closing its exit pathway (*SI Appendix*, Fig. S5 and Movie S2). These findings are consistent with the reduced Na^+ pumping efficiency of the E11A mutant (8) and with the inability of the R109A mutant to pump Na^+ (6, 7). It has been suggested that a glutamate residue homologous to Glu11 may be part of a proton release site in bR (32).

We also studied how the retinal reprotonation affects the dynamics of Na^+ in the transient binding site near Ser60/Ser64/Gln123 (site 1, Fig. 3*B*). In stark contrast to the simulations with the deprotonated retinal, where the ion ultimately exits to the cytoplasm, in four out of five independent simulations with a protonated retinal, the Na^+ ion is pulled toward the retinal, forming a contact with Asp116 (site 2, Fig. 3*B* and *SI Appendix*, Fig. S4*E*). This suggests that the negatively charged Asp116 may attract the Na^+ ion toward the retinal from the transient Ser60/Ser64/Gln123 binding site, in agreement with experiments suggesting that Na^+ is captured in the L/M → O transition (6).

To study whether Na^+ backflow could occur toward the intracellular side, we finally placed a Na^+ ion near the Glu11 residue in the extracellular water cavity of the equilibrated M state. In these simulations, the Na^+ ion rapidly leaves the extracellular cavity and enters the extracellular bulk solvent (*SI Appendix*, Fig. S4*F*), suggesting that the Na^+ ion is unlikely to spontaneously flow back to the intracellular side, even when the retinal is deprotonated. The behavior may be induced by the electrostatic repulsion caused by Arg109, indicating that the residue has a gating role in the pumping process (8), as also supported by the complete loss of Na^+ pumping activity of the R109A mutant (6). Although Na^+ does not spontaneously enter the protein cavities in our simulations, ion exchange with the bulk occurs as Na^+ exits the cavities (Fig. 3*A*).

Energetics of Na^+ Translocation. To probe the energetics of the Na^+ translocation, we calculated electrostatic solvation free-energy profiles of the ion in the putative KR2, K/L, and M states from continuous conduction pathways obtained from steered molecular dynamics (SMD) simulations, where the ion was pulled through the protein in each state. Although the electrostatic free energies do not explicitly include all entropic effects, we have performed calculations over several solvent and protein configurations to partly account for these effects (33). The transfer of Na^+ ions across the membrane to the extracellular side is energetically slightly exergonic, due to the overall negative surface charge of the protein on the extracellular side compared with the cytoplasmic side. For resting KR2, we obtain an energy barrier of ∼4 kcal·mol^{-1} for ion entry into the protein, followed by a local minimum at the Ser60/Ser64/Gln123 site (site 1), after which Leu120 provides another barrier, consistent with the MD simulations (Fig. 4). The Asp116 counterion stabilizes the Na^+ ion by a concerted rotation, similar to the movement of the protonated Asp116 in the M state (Fig. 2*A*), which leads to a local energy minimum at the Asn112/Asp116 site. The energy for conducting the Na^+ ion to Asp251 and Glu11 is energetically uphill by ∼5 kcal·mol^{-1}, suggesting that the ion would probably remain trapped in the middle of the protein. However, the relatively high barrier near the channel opening indicates that the ion uptake is unfavorable in resting KR2, as also predicted by the MD simulations, suggesting that the channel remains closed.

Formation of the K/L state leads to a strong decrease in the entry barrier for the Na^+ ion, and an overall exergonic transfer of ∼8 kcal·mol^{-1} of the ion to Asn112/Asp116, whereas Arg109 inhibits ion entry from the extracellular side. However, a large electrostatic barrier of ∼8 kcal·mol^{-1} prevents further transfer to the extracellular side via Asp251 and Glu11. The profile drastically changes upon formation of the M state, where a transition state forms at the Asn112/Asp116 site, followed by a downhill transfer to Asp251. The steep thermodynamic driving force toward site 3 arising from the electrostatic attraction of Asp251 (Fig. 4) could prevent the ion from being released back to the cytosol together with the dehydration occurring in the same transition (Fig. 2). In this state, the ion cannot pass the Arg109/Glu11 gate, but reprotonation followed by reisomerization of the retinal would lead to an exergonic transfer of the ion across the membrane (Fig. 4, dotted green line). This state would correspond to the O intermediate, suggesting that an all-*trans* retinal could facilitate ion release to the extracellular side. Because the O state is conformationally similar to the KR2 state, the barrier near the inside access point is also expected to prevent the ions from leaking toward the wrong side of the membrane. The role of electrostatic interactions in the ion translocation has also been shown to be important for halorhodopsin (hR) and bR (34).

Proton Transfer Energetics. To study the energetics of the proton transfer (pT) reactions between the PSB and Asp116, we calculated average pK_a values and QM/MM energy profiles for the pT in each relevant state. Our QM/MM profiles suggest that protonating Asp116 in the K/L state with no Na^+ present is endergonic by ∼0.5 kcal·mol^{-1} and has a barrier of 1.5 kcal·mol^{-1} (*SI Appendix*, Fig. S7). In addition, the average pK_a of Asp116 and the PSB are comparable in this state, indicating that proton transfer is energetically feasible. The pT is more endergonic by 2–4 kcal·mol^{-1} with Na^+ in site 2 (*SI Appendix*, Fig. S7), depending on the Asp116–Na^+ distance. The pK_a calculations also suggest that the pT can occur when Na^+ is not directly bound to Asp116 inside the cavity (*SI Appendix*, Fig. S8). The QM/MM profiles indicate that reprotonating the retinal in the M → O transition is endergonic by ∼1 kcal·mol^{-1}, suggesting that the pT is feasible with Na^+ in site 3, which is also supported by the pK_a calculations (*SI Appendix*, Table S3). Furthermore, the calculations show that the Na^+ is stabilized by 4–6 kcal·mol^{-1} when transferred from site 2 to site 3 in the K/L → M transition, in agreement with the electrostatic profiles (Fig. 4).

QM/MM Dynamics and Calculated Absorption Spectra for the Photocycle Intermediates. To characterize spectral signatures for our putative photocycle intermediates, we calculated vertical excitation energies (VEEs) and oscillator strengths for the retinal based on snapshots obtained from a 5-ps QM/MM MD simulation of each state (Fig. 5, *Materials and Methods*, and ref. 35). As the VEEs can be sensitive to the size of the QM model (36), all calculated spectra are reported relative to the experimental absorption maximum of dark-state KR2. Relative to the resting KR2 state at 526 nm (2.37 eV), we obtain a maximum at 530 nm for the K/L model that forms immediately after isomerization, i.e., when the Schiff base N-H bond vector points away from Asp116, and before the hydrogen bond between Asp116 and the PSB is reformed. The absorption

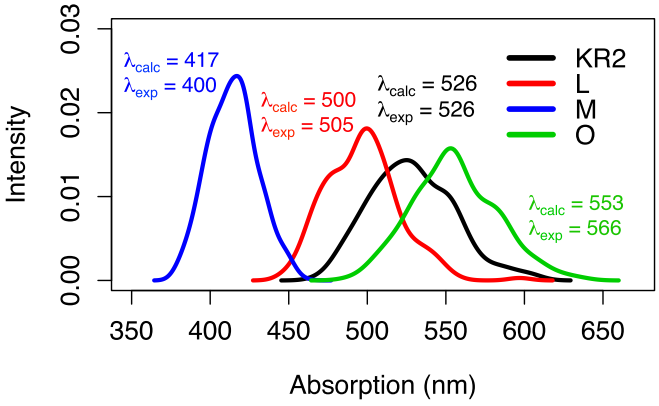

Fig. 5. Calculated absorption spectra and maxima of the photocycle intermediates. The spectra are calculated at the RVS-ADC(2)/def2-TZVP/CHARMM level of theory, based on 200 snapshots from 5-ps QM/MM MD simulations of each intermediate. In the O model, Na^+ is bound to Asn112/Asp116.

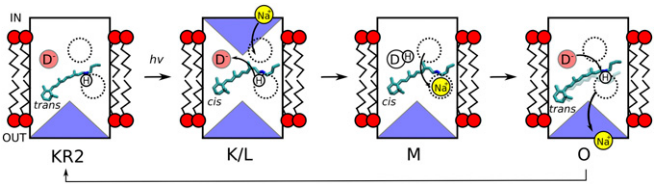

Fig. 6. Putative mechanism for the Na^+ translocation process. In the resting KR2 state, water connectivity between the retinal and the cytoplasm is inhibited. After the light-induced all-*trans* to 13-*cis* isomerization, the channel opens on the intracellular side, and Asp116, denoted by D, pulls the ion near the retinal. Proton transfer from the Schiff base to Asp116 forms the M intermediate, where the ion passes the retinal and enters the Asn112/Asp251 binding site. The intracellular portion of the channel is closed in M. Reprotonation and reisomerization form the O intermediate, where the ion is ejected to the extracellular side.

maximum of the K intermediate has not been experimentally determined, due to its fast decay during the photocycle (6), as also suggested by our MD simulations, but it is believed to be redshifted relative to the dark state as in other microbial rhodopsins. After the hydrogen bond between Asp116 and the PSB is reformed in K, the calculated absorption maximum blueshifts to 500 nm, which correlates very well with the L state, experimentally absorbing at 505 nm (6). For the M state, where the retinal is deprotonated, we obtain an absorption maximum at 417 nm, also in very good agreement with the experimental absorption maximum at 400 nm. We also investigated how Na^+ binding affects the absorption of M, but observe only a small shift to 414 nm with Na^+ bound to Asn112/Asp251, suggesting that Na^+ binding in the M state might lead to a very small shift in the absorption spectrum.

The experimental absorption maximum of the O state at 566 nm suggests that Na^+ is probably bound near the protonated retinal (6). We therefore calculated spectra for our K/L model with Na^+ bound to different sites to simulate the O state. With Na^+ bound to Asp116 in the intracellular water cavity (site 2, Fig. 3*B*) of the K/L state, the retinal absorbs at ∼510 nm, whereas the ion-free model absorbs at 500 nm. With the ion bound to the Asn112/Asp251 site in the K/L state, we obtain a maximum at 530 nm, which is also only slightly redshifted relative to the resting KR2 state. bR shows a highly redshifted O intermediate with an all-*trans* retinal (37). We therefore equilibrated a model of the resting KR2 state with an all-*trans* retinal and a Na^+ ion bound to the Asn112/Asp116 site, which has the lowest electrostatic energy according to our calculations (Fig. 4). Remarkably, this model absorbs at 553 nm, suggesting that the O intermediate could indeed also comprise an all-*trans* retinal similar to bR. Inoue et al. (6) observed two time decay rates for the O intermediate back to the resting KR2, which could originate from the decay of 13-*cis* and all-*trans* forms of the retinal. The significantly redshifted absorption of this intermediate also indicates that Na^+ is most likely not bound near the PSB in the resting KR2 state, as this would be apparent from the spectrum, for which no difference is observed when using NaCl or KCl (6, 7).

Mechanism of Na^+ Translocation. Based on the calculations, we can propose a minimal mechanistic model for the Na^+ translocation, schematically shown in Fig. 6. In the resting KR2 state, Na^+ is most likely not located near the PSB, as the electrostatic barrier for Na^+ transport along the channel is high, due to a closed conduction pathway (Fig. 4). After photon absorption and retinal isomerization, forming the K/L state, the hydrophobic gate at Leu120 opens up, allowing the Na^+ ion to approach Asp116, which is now positioned above the retinal in the intracellular cavity. The electrostatic interaction between Asp116 and the PSB, however, prevents the ion from accessing the Asn112/Asp251 binding site. Deprotonation of the retinal forms the M intermediate, where the Na^+ ion passes the neutral retinal, entering the Asn112/Asp251 site. As the Na^+ ion approaches Asn112/Asp251, Arg109 flips away from Asp251 toward Glu11 due to the electrostatic repulsion. Reprotonation and reisomerization of the retinal forms the O state, after which the Na^+ ion exits the binding site toward Glu11 at the extracellular opening and leaves the protein. As the Na^+ ion leaves the binding site, Arg109 flips back toward Asp251, preventing backflow of the ion toward its thermodynamically favorable direction. The system is thus returned to the resting KR2 state and is ready for the next photocycle upon arrival of a photon.

Conclusions

We have shown here using extensive classical MD simulations and QM/MM calculations how internal conformational dynamics and proton transfer reactions induce electrostatic transitions that activate the Na^+ pumping. We found that hydration effects likely play an important role in the Na^+ translocation, and we identified several key residues that provide important gating elements in the process. Remarkably, similar combined electrostatically triggered conformational and hydration changes have recently been observed in several energy converting proteins such as the respiratory complex I (38, 39). We also spectrally characterize the transient photocycle states and suggest putative structures for each intermediate. Our combined results on the dynamics and energetics of the Na^+ translocation process can stimulate new site-directed mutagenesis experiments and provide a basis for modifying KR2 toward neurobiological applications.

Materials and Methods

Classical MD simulations were prepared based on the X-ray structure of KR2 from *K. eikastus* [Protein Data Bank (PDB) ID code 3X3B] (7). For the resting state, all amino acid residues were modeled in their standard protonation states. The protein was embedded in a 1,2-dimyristoyl-*sn*-glycero-3-phosphocholine (DMPC) membrane, surrounded by a water box, and neutralized by adding 150 mM NaCl. The system, comprising 55,708 atoms, was simulated at 310 K using a 2-fs timestep and *NPT* conditions with the CHARMM27 force field (40) and retinal parameters obtained from Hayashi et al. (41–45). Long-range electrostatic forces were treated using the particle-mesh Ewald (PME) method. After 1.5 μs of simulating the resting state, we prepared the K/L state by rotating the dihedral angle around C13 and C14 of the retinal to form 13-*cis* retinal. After a 1.5-μs MD simulation of the K/L state, the M state was prepared by transferring the Schiff base proton to Asp116. The simulations of the K/L and M states were repeated five times. SMD simulations were performed to obtain a continuous Na^+ conduction pathway (*SI Appendix*).

Hybrid QM/MM calculations were performed with the retinal and Asp116 in the quantum (QM) region, which was treated at the B3LYP-D3/def2-SVP (46–49) level. The systems were optimized for 100 steps, after which QM/MM MD simulations were performed for 5 ps using a 1-fs timestep. VEEs and oscillator strengths were calculated using the same QM region for snapshots taken at 25-fs intervals from the QM/MM MD trajectories using the algebraic-diagrammatic construction through second-order [ADC(2)] (50) method in combination with the reduced virtual space (RVS) (51) approach with an RVS threshold of 50 eV and def2-TZVP basis sets. The spectra were weighted with the oscillator strengths and smoothed using Gaussian kernel density estimation.

NAMD2 (52) was used for all classical MD simulations and the CHARMM/TURBOMOLE interface (53–55) was used for the QM/MM calculations. Solvation free energies were computed for ∼700 frames obtained from the SMD simulations using Poisson–Boltzmann continuum electrostatics in MEAD (56, 57). The Na^+ ion, the protein, and the membrane were modeled using atomic partial charges with a low dielectric constant ($\varepsilon = 4$) and bulk water as a continuum with a high dielectric constant ($\varepsilon = 80$). The results were averaged using local polynomial regression fitting, with a residual SE of ∼1.0 kcal·mol^{-1}. pK_a calculations were performed using APBS (58) with the setup described above. All titratable residues were sampled using the Monte Carlo procedure in Karlsberg+, for which a benchmarked accuracy of ∼1 pK_a unit has been found (59–61). VMD (62) was used for analysis and visualization. Details of the simulation setups are summarized in *SI Appendix*, Table S1.

ACKNOWLEDGMENTS. C.-M.S. is supported by the Doctoral Programme in Chemistry and Molecular Sciences (University of Helsinki). This research was supported by the European Research Council (V.R.I.K.), the German Academic Exchange Service–Finnish Academy (287791 to V.R.I.K. and D.S.), the Magnus Ehrnrooth Foundation (D.S.), and the Academy of Finland (275845 to D.S.). The Finnish Information Technology Center for Science and the Leibniz Supercomputing Centre provided computational resources.

1. Kaila VRI, Verkhovsky MI, Wikström M (2010) Proton-coupled electron transfer in cytochrome oxidase. *Chem Rev* 110:7062–7081.
2. Cardona T, Sedoud A, Cox N, Rutherford AW (2012) Charge separation in photosystem II: A comparative and evolutionary overview. *Biochim Biophys Acta* 1817:26–43.
3. Mitchell P, Moyle J (1967) Chemiosmotic hypothesis of oxidative phosphorylation. *Nature* 213:137–139.
4. Yoshida M, Muneyuki E, Hisabori T (2001) ATP synthase: A marvellous rotary engine of the cell. *Nat Rev Mol Cell Biol* 2:669–677.
5. Ernst OP, et al. (2014) Microbial and animal rhodopsins: Structures, functions, and molecular mechanisms. *Chem Rev* 114:126–163.
6. Inoue K, et al. (2013) A light-driven sodium ion pump in marine bacteria. *Nat Commun* 4:1678.
7. Kato HE, et al. (2015) Structural basis for Na(+) transport mechanism by a light-driven Na(+) pump. *Nature* 521:48–53.
8. Gushchin I, et al. (2015) Crystal structure of a light-driven sodium pump. *Nat Struct Mol Biol* 22:390–395.
9. da Silva GF, Goblirsch BR, Tsai AL, Spudich JL (2015) Cation-specific conformations in a dual-function ion-pumping microbial rhodopsin. *Biochemistry* 54:3950–3959.
10. Inoue K, Konno M, Abe-Yoshizumi R, Kandori H (2015) The role of the NDQ motif in sodium-pumping rhodopsins. *Angew Chem Int Ed Engl* 54:11536–11539.
11. Kato Y, Inoue K, Kandori H (2015) Kinetic analysis of H(+)-Na(+) selectivity in a light-driven Na(+)-pumping rhodopsin. *J Phys Chem Lett* 6:5111–5115.
12. Bogachev AV, Bertsova YV, Verkhovskaya ML, Mamedov MD, Skulachev VP (2016) Real-time kinetics of electrogenic Na(+) transport by rhodopsin from the marine flavobacterium Dokdonia sp. PRO95. *Sci Rep* 6:21397.
13. Boyden ES, Zhang F, Bamberg E, Nagel G, Deisseroth K (2005) Millisecond-timescale, genetically targeted optical control of neural activity. *Nat Neurosci* 8:1263–1268.
14. Hoque MR, et al. (2016) A chimera Na+-pump rhodopsin as an effective optogenetic silencer. *PLoS One* 11:e0166820.
15. Ono H, Inoue K, Abe-Yoshizumi R, Kandori H (2014) FTIR spectroscopy of a light-driven compatible sodium ion-proton pumping rhodopsin at 77 K. *J Phys Chem B* 118:4784–4792.
16. Tahara S, et al. (2015) Ultrafast photoreaction dynamics of a light-driven sodium-ion-pumping retinal protein from Krokinobacter eikastus revealed by femtosecond time-resolved absorption spectroscopy. *J Phys Chem Lett* 6:4481–4486.
17. Hontani Y, et al. (2016) The photochemistry of sodium ion pump rhodopsin observed by watermarked femto- to submillisecond stimulated Raman spectroscopy. *Phys Chem Chem Phys* 18:24729–24736.
18. Shigeta A, et al. (2017) Solid-state nuclear magnetic resonance structural study of the retinal-binding pocket in sodium ion pump rhodopsin. *Biochemistry* 56:543–550.
19. Luecke H, et al. (2008) Crystallographic structure of xanthorhodopsin, the light-driven proton pump with a dual chromophore. *Proc Natl Acad Sci USA* 105:16561–16565.
20. Kouyama T, et al. (2014) Structure of archaerhodopsin-2 at 1.8-Å resolution. *Acta Crystallogr D Biol Crystallogr* 70:2692–2701.
21. Kim K, et al. (2016) Crystal structure and functional characterization of a light-driven chloride pump having an NTQ motif. *Nat Commun* 7:12677.
22. Hosaka T, et al. (2016) Structural mechanism for light-driven transport by a new type of chloride ion pump, Nonlabens marinus Rhodopsin-3. *J Biol Chem* 291:17488–17495.
23. Konno M, et al. (2016) Mutant of a light-driven sodium ion pump can transport cesium ions. *J Phys Chem Lett* 7:51–55.
24. Freier E, Wolf S, Gerwert K (2011) Proton transfer via a transient linear water-molecule chain in a membrane protein. *Proc Natl Acad Sci USA* 108:11435–11439.
25. Garczarek F, Gerwert K (2006) Functional waters in intraprotein proton transfer monitored by FTIR difference spectroscopy. *Nature* 439:109–112.
26. Kouyama T, Nishikawa T, Tokuhisa T, Okumura H (2004) Crystal structure of the L intermediate of bacteriorhodopsin: Evidence for vertical translocation of a water molecule during the proton pumping cycle. *J Mol Biol* 335:531–546.
27. Subramaniam S, Greenhalgh DA, Rath P, Rothschild KJ, Khorana HG (1991) Replacement of leucine-93 by alanine or threonine slows down the decay of the N and O intermediates in the photocycle of bacteriorhodopsin: Implications for proton uptake and 13-cis-retinal–all-trans-retinal reisomerization. *Proc Natl Acad Sci USA* 88:6873–6877.
28. Lórenz-Fonfría VA, et al. (2015) Temporal evolution of helix hydration in a light-gated ion channel correlates with ion conductance. *Proc Natl Acad Sci USA* 112: E5796–E5804.
29. Kuhne J, et al. (2015) Early formation of the ion-conducting pore in channelrhodopsin-2. *Angew Chem Int Ed Engl* 54:4953–4957.
30. Abe-Yoshizumi R, Inoue K, Kato HE, Nureki O, Kandori H (2016) Role of Asn112 in a light-driven sodium ion-pumping rhodopsin. *Biochemistry* 55:5790–5797.
31. Mamedov MD, Mamedov AM, Bertsova YV, Bogachev AV (2016) A single mutation converts bacterial Na(+)-transporting rhodopsin into an H(+) transporter. *FEBS Lett* 590: 2827–2835.
32. Phatak P, Ghosh N, Yu H, Cui Q, Elstner M (2008) Amino acids with an intermolecular proton bond as proton storage site in bacteriorhodopsin. *Proc Natl Acad Sci USA* 105: 19672–19677.
33. Genheden S, Ryde U (2015) The MM/PBSA and MM/GBSA methods to estimate ligand-binding affinities. *Expert Opin Drug Discov* 10:449–461.
34. Song Y, Gunner MR (2014) Halorhodopsin pumps Cl^- and bacteriorhodopsin pumps protons by a common mechanism that uses conserved electrostatic interactions. *Proc Natl Acad Sci USA* 111:16377–16382.
35. Gamiz-Hernandez AP, Kaila VRI (2016) Conversion of light-energy into molecular strain in the photocycle of the photoactive yellow protein. *Phys Chem Chem Phys* 18:2802–2809.
36. Suomivuori CM, Lang L, Sundholm D, Gamiz-Hernandez AP, Kaila VRI (2016) Tuning the protein-induced absorption shifts of retinal in engineered rhodopsin mimics. *Chem Eur J* 22:8254–8261.
37. Wickstrand C, Dods R, Royant A, Neutze R (2015) Bacteriorhodopsin: Would the real structural intermediates please stand up? *Biochim Biophys Acta* 1850:536–553.
38. Kaila VRI, Wikström M, Hummer G (2014) Electrostatics, hydration, and proton transfer dynamics in the membrane domain of respiratory complex I. *Proc Natl Acad Sci USA* 111:6988–6993.
39. Sharma V, et al. (2015) Redox-induced activation of the proton pump in the respiratory complex I. *Proc Natl Acad Sci USA* 112:11571–11576.
40. MacKerell AD, et al. (1998) All-atom empirical potential for molecular modeling and dynamics studies of proteins. *J Phys Chem B* 102:3586–3616.
41. Nina M, Roux B, Smith JC (1995) Functional interactions in bacteriorhodopsin: A theoretical analysis of retinal hydrogen bonding with water. *Biophys J* 68:25–39.
42. Tajkhorshid E, Paizs B, Suhai S (1997) Conformational effects on the proton affinity of the Schiff base in bacteriorhodopsin: A density functional study. *J Phys Chem B* 101:8021–8028.
43. Tajkhorshid E, Suhai S (1999) Influence of the methyl groups on the structure, charge distribution, and proton affinity of the retinal Schiff base. *J Phys Chem B* 103:5581–5590.
44. Hayashi S, Ohmine I (2000) Proton transfer in bacteriorhodopsin: Structure, excitation, IR spectra, and potential energy surface analyses by an ab initio QM/MM method. *J Phys Chem B* 104:10678–10691.
45. Hayashi S, et al. (2001) Structural determinants of spectral tuning in retinal proteins bacteriorhodopsin vs sensory rhodopsin II. *J Phys Chem B* 105:10124–10131.
46. Lee C, Yang W, Parr RG (1988) Development of the Colle-Salvetti correlation-energy formula into a functional of the electron density. *Phys Rev B Condens Matter* 37:785–789.
47. Becke AD (1993) Density-functional thermochemistry. III. The role of exact exchange. *J Chem Phys* 98:5648–5652.
48. Weigend F, Ahlrichs R (2005) Balanced basis sets of split valence, triple zeta valence and quadruple zeta valence quality for H to Rn: Design and assessment of accuracy. *Phys Chem Chem Phys* 7:3297–3305.
49. Grimme S, Antony J, Ehrlich S, Krieg H (2010) A consistent and accurate ab initio parametrization of density functional dispersion correction (DFT-D) for the 94 elements H-Pu. *J Chem Phys* 132:154104.
50. Trofimov AB, Schirmer J (1995) An efficient polarization propagator approach to valence electron excitation spectra. *J Phys At Mol Opt Phys* 28:2299.
51. Send R, Kaila VRI, Sundholm D (2011) Reduction of the virtual space for coupled-cluster excitation energies of large molecules and embedded systems. *J Chem Phys* 134:214114.
52. Phillips JC, et al. (2005) Scalable molecular dynamics with NAMD. *J Comput Chem* 26: 1781–1802.
53. Ahlrichs R, Bär M, Häser M, Horn H, Kölmel C (1989) Electronic structure calculations on workstation computers: The program system TURBOMOLE. *Chem Phys Lett* 162:165–169.
54. Brooks BR, et al. (2009) CHARMM: The biomolecular simulation program. *J Comput Chem* 30:1545–1614.
55. Riahi S, Rowley CN (2014) The CHARMM-TURBOMOLE interface for efficient and accurate QM/MM molecular dynamics, free energies, and excited state properties. *J Comput Chem* 35:2076–2086.
56. Bashford D, Gerwert K (1992) Electrostatic calculations of the pKa values of ionizable groups in bacteriorhodopsin. *J Mol Biol* 224:473–486.
57. Bashford D (1997) An object-oriented programming suite for electrostatic effects in biological molecules: An experience report on the MEAD project. *International Conference on Computing in Object-Oriented Parallel Environments* (Springer, New York), pp 233–240.
58. Baker NA, Sept D, Joseph S, Holst MJ, McCammon JA (2001) Electrostatics of nanosystems: Application to microtubules and the ribosome. *Proc Natl Acad Sci USA* 98:10037–10041.
59. Sheves M, Albeck A, Friedman N, Ottolenghi M (1986) Controlling the pKa of the bacteriorhodopsin Schiff base by use of artificial retinal analogues. *Proc Natl Acad Sci USA* 83:3262–3266.
60. Rabenstein B, Knapp E-W (2001) Calculated pH-dependent population and protonation of carbon-monoxy-myoglobin conformers. *Biophys J* 80:1141–1150.
61. Kieseritzky G, Knapp EW (2008) Optimizing pKa computation in proteins with pH adapted conformations. *Proteins* 71:1335–1348.
62. Humphrey W, Dalke A, Schulten K (1996) VMD: Visual molecular dynamics. *J Mol Graph* 14:33–38, 27–28.